

Constructing nano-object quantum superpositions with a Stern-Gerlach interferometer

Ryan J. Marshman¹, Anupam Mazumdar², Ron Folman³, and Sougato Bose¹

¹*Department of Physics and Astronomy, University College London, Gower Street, WC1E 6BT London, United Kingdom*

²*Van Swinderen Institute, University of Groningen, 9747 AG Groningen, Netherlands*

³*Department of Physics, Ben-Gurion University of the Negev, Be'er Sheva 84105, Israel*



(Received 27 June 2021; accepted 21 January 2022; published 2 May 2022)

Probing quantum mechanics and quantum aspects of general relativity, along with the sensing and constraining of classical gravity, can all be enabled by unprecedented spatial sizes of superpositions of massive objects. In this paper, we show that there is a feasible setup sourced by realizable magnetic field gradients $O(10\text{--}100)\text{ T m}^{-1}$ to construct a large spatial superposition of $O(10^{-4}\text{--}10^{-8})\text{ m}$ for $O(10^{-17}\text{--}10^{-14})\text{ kg}$ masses within a time of up to $0.1\text{--}10$ seconds. The scale of superpositions is unrestricted as long as quantum coherence can be maintained for a required amount of time.

DOI: [10.1103/PhysRevResearch.4.023087](https://doi.org/10.1103/PhysRevResearch.4.023087)

I. INTRODUCTION

At a microscopic level, three of the known forces of nature, electromagnetic (EM), weak, and strong, obey the principles of local quantum field theory (QFT) [1]. However, there is no experimental proof yet of *how* the gravitational interaction is being mediated. Recently, a tabletop experiment has been suggested to explore the quantum origin of gravity [2–4]. The protocol crucially relies on the interaction of quantum matter with quantum gravity, leading to the generation of entanglement between spins embedded in two nonrelativistic test masses [3]. The spin entanglement witness will prove the graviton’s quantumness as a mediator of the force between the two masses (quantumness of the linearized metric fluctuations around a Minkowski background), and will further test the nature of the gravitational interaction at microscopic distances [3,5]. However, there remains a demanding requirement: *quantum spatial superpositions of distinct localized states of neutral mesoscopic masses* $m \sim 10^{-15}\text{ kg}$ over spatial separations of $\Delta x \sim 10\ \mu\text{m}$ [6], far beyond the scales achieved to date (e.g., macromolecules $m \sim 10^{-22}\text{ kg}$ over $\Delta x \sim 0.25\ \mu\text{m}$, or atoms $m \sim 10^{-25}\text{ kg}$ over $\Delta x \sim 0.5\text{ m}$) [7,8]. Such superpositions have also been shown to be of practical value in sensing of weak forces, curvature [9], frame dragging, and even a tabletop detection of low-frequency gravitational waves [10].

Beyond the usage in sensing quantum and classical gravity, upgrading the mass m and the superposition Δx naturally stretches the boundaries of the validity of quantum mechanics (QM), which in itself is a worthy goal [8,11]. However, there is a gap in the literature at the moment as far as a realistic

scheme for achieving superposition sizes $\Delta x > 1\ \mu\text{m}$. While there are quite a few schemes for a lower Δx or m investigated at various levels of detail [12–32], and while these may suffice to falsify various purported modifications of QM [33–35], the only two predictions stemming from the straightforward application of QM (local QFT to be more precise [3]) which would give us nontrivial information (e.g., sensing the quantum nature of gravity [2] and sensing extremely weak classical gravity [10]) necessarily seem to require $\Delta x \gtrsim 1\ \mu\text{m}$.

Rudimentary arguments on how to achieve such superpositions using a Stern-Gerlach interferometer (SGI) in high magnetic field gradients were presented in [2], building on earlier ideas for smaller m , Δx superpositions [20,36]. A feasibility study building on atomic experiments was recently performed, showing that SGI for massive objects is indeed possible [31]. However, beyond a simple scaling of mass, little work has been done [29] on exploring what new issues will arise when these techniques are pushed beyond the atomic level.

In this paper, we go further in several respects by incorporating some crucial aspects missed in previous treatments while making it simultaneously less demanding in certain aspects, and confirm the true potential for the spatial splitting of massive objects (namely nanocrystals) achieved by SGI. The proposal outlined here requires only moderate magnetic gradients, significantly less than what was originally considered necessary [2] as shown in Fig. 3. We will be describing a 1D longitudinal interferometer, which avoids the problems noted for 2D interferometers [37]. We take into account gradients in other directions, as demanded by Maxwell equations. We take into account the effects of the induced diamagnetism within the interferometric mass as while this is not of concern with atomic Stern-Gerlach interferometry, it becomes a dominant effect once larger masses are considered. We consider a magnetic source which enables constant gradients over a large volume. In contrast to the previous works [19,20,29], we have a scheme without a low magnetic field in any region, so as to avoid the historically well-known phenomenon of Majorana

Published by the American Physical Society under the terms of the [Creative Commons Attribution 4.0 International](https://creativecommons.org/licenses/by/4.0/) license. Further distribution of this work must maintain attribution to the author(s) and the published article’s title, journal citation, and DOI.

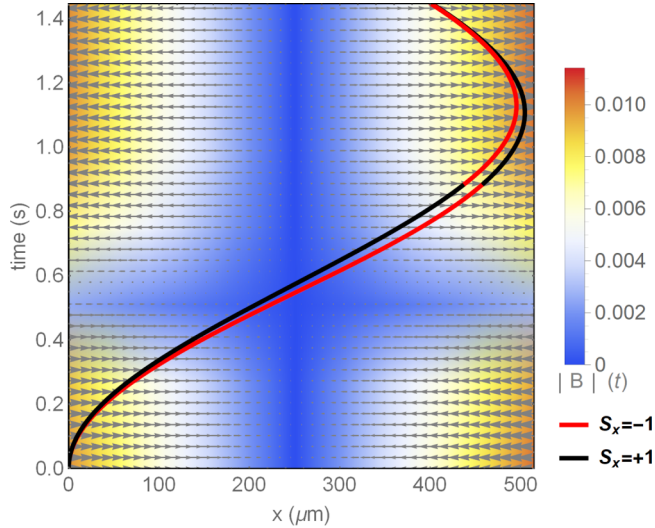


FIG. 1. Example interferometer path trajectories through the varying magnetic fields used. The magnetic field transition time here is accentuated for readability. Note that the internal spin states are reversed at time $t \approx 0.9$ s to ensure the interferometer is closed.

spin flips [38,39]. In this way we have *combined* well-studied problems in particle trapping (Majorana spin flips), and practical realizations of the Stern-Gerlach effect to show that a full-loop interferometer [31], where wave packets are spatially split in a spin-dependent manner and then brought back to overlap both in position and momentum to complete the interferometry, is still possible with nanocrystals.

The above results are *simultaneously* achieved by a significant modification of standard SGI by changing the initial conditions and incorporating a gradient-free spatial region in which the diamagnetic force does not act, and yet, the superposition continues to grow in view of a momentum difference. However, we show what appears to be an unavoidable price to pay, which is a linear growth of a relative phase between the superposed components in time. These features allow us to present in detail a feasible interferometric accelerator for microscale masses, and enable the creation of a massive Schrödinger's cat.

Previous experimental configurations consider a magnetic field which originates in a single current-carrying wire or a permanent magnet, whereby the field goes as $\vec{B} \propto 1/r$, where r is the distance from the source. The magnetic field can then be linearized in a small region within which it has an approximately constant gradient. However, a large splitting will require long evolution times, and as the distance quickly increases between the particle and the wire, significant magnetic gradients are no longer available. We will therefore consider a configuration which enables a constant gradient over a large region (e.g., quadrupole field from coils in an anti-Helmholtz configuration). A typical resultant trajectory of such a potential is shown in Fig. 1.

II. MODEL

We assume a host nanocrystal with a single spin embedded in it, and concentrate, in this work, only on the translational

motion of this crystal under a magnetic field gradient. To explicitly model the spin and the host crystal material, we will assume a nitrogen-vacancy (NV) center spin in a diamond nano/microcrystal, although this analysis holds for all materials with similar diamagnetic susceptibilities and generic electronic spins. We consider the mass to be in a *free fall* along the z axis. We therefore do not treat its motion along the z axis explicitly as here the z motion commutes with the motion along the other two axes. Moreover, z motion would be absent in a drop-tower experiment, for example, which may be necessary in such experiments because of their long durations of ~ 1 s, and to mitigate gravitational jitters [9]. The Hamiltonian of the system is given by [29,40]

$$H = \frac{\hat{p}_x^2 + \hat{p}_y^2 + \hat{p}_z^2}{2m} + \hbar D \hat{S}_x^2 - \frac{\chi_m m}{2\mu_0} \vec{B}^2 - \mu_B \hat{s} \cdot \vec{B}, \quad (1)$$

where m is the mass of the diamond, $\chi_m = -6.2 \times 10^{-9} \text{ m}^3 \text{ kg}^{-1}$ is the mass magnetic susceptibility, μ_B is the Bohr magneton, \hat{s} is the spin operator, and $D = (2\pi) \times 2.8 \text{ GHz}$ is the NV zero-field splitting. Note that in writing the above Hamiltonian, we are only concentrating on the *translational motion*; we are assuming that we can engineer a situation so that the torque and the rotational effects of the mass are negligible/decoupled from translation (for possible mechanisms to cool rotation, see [41–44]). The external magnetic field \vec{B} varies in the x - y plane, and as we will see, with our choice of its profile, couples predominantly to the x motion via the x component of the spin. Under this setting, once the internal spin of the NV center is initialized in the state $\frac{1}{\sqrt{2}}(|1\rangle + |-1\rangle)$, we will realize a 1-dimensional SGI which, as time progresses, achieves first a maximum wave function splitting Δx in the x direction, and then, via appropriate spin flips/magnetic gradient changes, its subsequent recombination to complete the interferometry. The second term of the Hamiltonian drops out as a common phase and we will omit this term from our analysis. This also means that our results will be completely general, and hold for other (say spin-1/2) dopants in generic crystals.

There are known predicaments for generating superpositions by using a spin coupled to a magnetic field: (1) The electronic spin will in general experience Majorana spin flips whenever the magnetic field magnitude becomes small, thus no longer remaining in a well-defined eigenstate as required for the coherent manipulation of the masses (this is particularly important for our results to be inclusive of generic spin dopant atoms in a nanocrystal; it has been perceived as an important problem for several atomic species [39]). (2) Another is the effect of off-axis magnetic field gradients, which are generally not considered [29]; however, this *must* be taken into account to satisfy Maxwell's equations.

First, we will consider the constraints on the magnetic field to address the above problems. Note that $\vec{\nabla} \cdot \vec{B} = 0$ and $\vec{\nabla} \times \vec{B} = 0$, as we keep the mass away from the source of the magnetic field. For simplicity, we assume the following profile in the (x, y) plane: $\vec{B} = B_x(x, y)\hat{x} + B_y(x, y)\hat{y}$. We take the x axis as the *desired superposition direction*, and we require the magnetic field to be linear along the x direction, with a constant magnetic field gradient along the x direction to take some constant value ∂B . To ensure that we can take the x

axis as our quantization axis, and that Majorana spin flips are avoided, we require that $|B_x(x, y)| \gg |B_y(x, y)| \forall x, y$ in the vicinity of the controlled trajectories. The simplest general form for the magnetic field which will satisfy all the above conditions can be given by

$$\vec{B}(x, y) = [B_x(0, 0) - \partial B_x]\hat{x} + \partial B_y\hat{y}, \quad (2)$$

for any fixed value of the magnetic field at the origin $B_x(0, 0)$ and magnetic field gradient ∂B . Note that for positive $B_x(0, 0)$ and ∂B the zero point of the magnetic field is always on the positive x axis. By ensuring that $y \approx 0$ during the entire interferometry, we find a suitable definition for the zero magnetic field region which must be avoided of

$$x \notin \left[\frac{B_x(0, 0) - \varepsilon}{\partial B}, \frac{B_x(0, 0) + \varepsilon}{\partial B} \right], \quad (3)$$

where ε is the minimum allowable magnetic field in the x direction. For a sufficiently large ε , we can ascertain that the spin states will always be approximately aligned along the quantization (x) axis and Majorana spin flips are avoided.

The spin state in the y and z basis will experience a rapid Larmor precession, with a frequency set by $\omega_L = -\frac{ge}{2m_e}|B(x, y)|$, where $g \approx 2$ is here the Landé g factor, e is the electron charge, and m_e is the electron mass. If we desire a minimum Larmor frequency of ω_L^{\min} , we can define a minimum allowable magnetic field magnitude:

$$\varepsilon \sim -\frac{2m_e\omega_L^{\min}}{ge}. \quad (4)$$

Therefore, the particle must not enter the region given by Eq. (3). To achieve this, we will use three linear magnetic field profiles sequentially in time, which are specific solutions of the form of Eq. (2):

$$\vec{B}(x, y) = (B_0 - \eta x)\hat{x} + \eta y\hat{y}, \quad (5)$$

$$\vec{B}(x, y) = B_1\hat{x}, \quad (6)$$

$$\vec{B}(x, y) = -(B_0 - \eta x)\hat{x} - \eta y\hat{y}, \quad (7)$$

with $B_0, B_1, \eta > 0$. We then require $B_1 \gg \varepsilon$, and the timing of the switching between the magnetic fields will be done to ensure that the particle never experiences a small magnetic field. That is, as the particle approaches the disallowed region given by Eq. (3) [for $B_x(0, 0) = B_0$ and $\partial B = \eta$], the magnetic field is mapped to that given by Eq. (6) [where now $B_x(0, 0) = B_1$ and $\partial B = 0$, and thus the region specified by Eq. (3) does not occur], and as it leaves that region, the magnetic field is smoothly mapped to Eq. (7) [where $B_x(0, 0) = -B_0$ and $\partial B = -\eta$]. The switching function will be modeled by $\text{Sw}(t, t_{\text{on}}, t_{\text{off}}) = 0.5\{\tanh[\delta(t - t_{\text{on}})] + 1\} \times 0.5\{\tanh[\delta(t_{\text{off}} - t)] + 1\}$, where δ is the switching frequency parameter, which we ensure to be sufficiently slow such that the magnetic field change is always adiabatic. This is to ensure that it does not complicate the spin dynamics. We consider $\delta = 10^3$ Hz, which is well below what is required to maintain the adiabaticity conditions $\dot{\omega}_L/\omega_L^2 \ll 1$ and $\delta \ll \omega_L^{\min}$. With this, since the magnetic field is along a fixed direction, it effectively freezes the spin direction (with the other spin

components experiencing high-frequency Larmor precession) ensuring the interferometer is *effectively* one-dimensional.

The motion of the particle can be separated into different stages, largely depending on the form of \vec{B} :

- (1) $t < \tau_1$: \vec{B} is given by Eq. (5).
- (2) $\tau_1 \leq t < \tau_2$: \vec{B} is switching adiabatically from Eq. (5) to Eq. (6), via the switching function $\text{Sw}(t, t_{\text{on}}, t_{\text{off}})$.
- (3) $\tau_2 \leq t < \tau_3$: \vec{B} is given by Eq. (6).
- (4) $\tau_3 \leq t < \tau_4$: \vec{B} is switching adiabatically from Eq. (6) to Eq. (7) via the switching function $\text{Sw}(t, t_{\text{on}}, t_{\text{off}})$.
- (5) $\tau_4 \leq t$: \vec{B} is given by Eq. (7).
- (6) $t = \tau_5$: When the spin states are reversed to close the superposition while \vec{B} is still given by Eq. (7).
- (7) $t = \tau_6$: When the two wave functions are brought to overlap in the position and the momentum basis.

Away from the nearly zero-field region, where the magnetic field profile is given by Eq. (5) or (7), we can write the potential energy in a compact form as

$$U_{\pm}(\tilde{x}') = -\frac{\chi_m m}{2\mu_0} \eta^2 \tilde{x}'^2 + \mu_{\pm} \frac{\mu_0}{\chi_m m}, \quad (8)$$

where we have taken $y \approx 0$, while the second term is a constant energy, and $\tilde{x}' = x - C(s_x)$, where

$$C(s_x = \pm 1) = B_0/\eta \pm \frac{ge\hbar}{2m_e} \frac{\mu_0}{\chi_m m \tilde{\eta}(t)}, \quad (9)$$

where $\tilde{\eta}(t) = \eta$ when $t < \tau_1$ and $\tilde{\eta}(t) = -\eta$ when $t > \tau_4$. Thus the object sees a harmonic potential created by the diamagnetic interaction whose center is displaced in the x direction by the spin-magnetic field gradient interaction. It is clear from the above that the object will roll in different potential wells corresponding to its spin state and thereby develop a momentum difference as they approach the nearly zero-field region. It is in this region that we switch the gradient (the harmonic potential) off, and let the object evolve in a magnetic field given by Eq. (6) so that a continually increasing spatial splitting can develop due to the momentum difference of the spin components, while Majorana spin flips are avoided. When the masses are in a coherent state of the harmonic potential, the wave function will not spread, while when in the constant magnetic field (free motion) it will hardly spread due to the largeness of the mass. Thus, it suffices to model the center of mass as following a classical trajectory for each interferometric path. Thermal fluctuations in the initial state do not limit the coherence in the final state as they factor out of the motion; see the discussions in [12,20]. To a good approximation, the two interferometric paths can be modeled by $x(t) = A \cos(\omega t + \phi) + C(s_x)$, where the frequency of the diamagnetic trap is given by $\omega = (-\chi_m/\mu_0)^{1/2}\eta$, while note that $\chi_m < 0$ as the mass is diamagnetic. This leaves the amplitude A and the phase ϕ to be determined by requiring that the position and the momentum of each arm of the interferometer are continuous throughout the trajectory. For the ease of computation, we have solved the complete trajectories using an appropriate combination of analytic and numerical solutions. For periods of evolution by a time-independent Hamiltonian, analytic solutions are used. However to allow for a more realistic magnetic field switching to be modeled, numerics are used, specifically during $\tau_1 \leq t < \tau_2$ and $\tau_3 \leq t < \tau_4$. This is discussed in more detail in the Appendix. The resulting

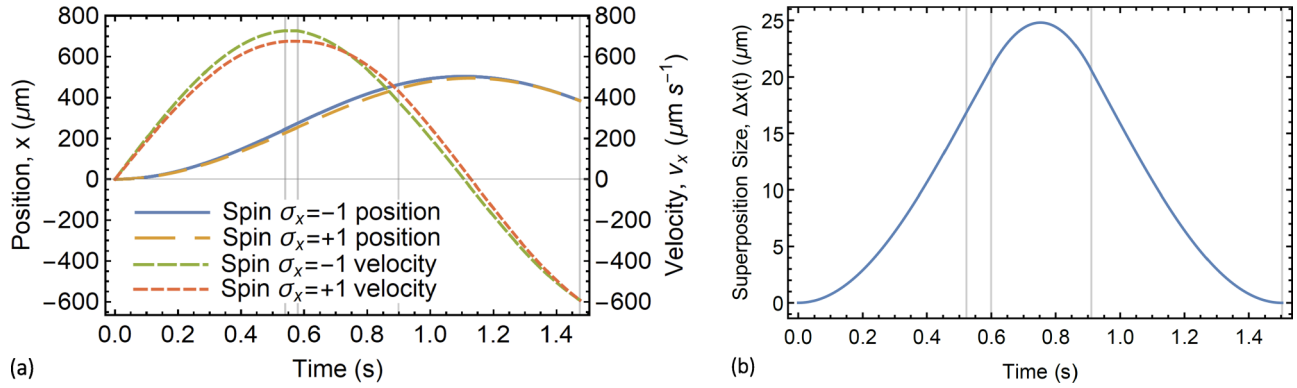


FIG. 2. Panel (a) shows both the paths taken through the interferometer and the corresponding velocity while panel (b) shows the superposition size with time. These plots are the result of the combined numerical and analytical analysis. The vertical gray lines represent times $\tau_1 \approx \tau_2$, $\tau_3 \approx \tau_4$, τ_5 , and τ_6 . Both figures are for $B_0 = 10^{-2}$ T, $\eta = 46.483$ T m $^{-1}$, and $m = 10^{-17}$ kg.

motion can be seen in Fig. 2. Note that at $\tau_5 \approx 0.9$ s (marked by the vertical lines in Fig. 2), the spin reversal takes place by firing a rapid microwave pulse to alter the internal spin state. We can find numerically the final time τ_6 to be

$$\tau_6 \approx 59 \times (1 \text{ T m}^{-1} / \eta) \text{ sec}, \quad (10)$$

to ensure that the relative positions of the two paths $\Delta x(t = \tau_6) \approx 0$ m, and the relative velocity $\Delta v(t = \tau_6) \approx 0$ m s $^{-1}$ (completion of interferometry).

This results in the superposition sizes as seen in Fig. 3, and the trajectories through the interferometer can be seen as in Fig. 2. Furthermore, the maximum superposition which occurs between $\tau_4 < t < \tau_5$ can be determined numerically:

$$\Delta x_{\max}(m, \tau_6) \approx \left(\frac{1.6 \times 10^{-16} \text{ kg}}{m} \right) \left(\frac{\tau_6}{1 \text{ sec}} \right) \times 10^{-6} \text{ m} \quad (11)$$

for $B_0 = 10^{-2}$ T, $B_1 = 100\epsilon$, and $m \gtrsim 10^{-17}$ kg. The latter condition on the mass arises because smaller masses are subject to much smaller induced diamagnetic potential. For a lighter diamond, if we do not modify the times $\tau_i(\eta)$ and B_1 , the masses would inevitably move through the zero-field region of the magnetic field, and this therefore demands a different magnetic field setup; see [31,45]. Therefore, our analysis holds true for $m \gtrsim 10^{-17}$ kg for $\chi_m \approx -6.2 \times$

10^{-9} kg m $^{-3}$. Using Eq. (11) we can estimate that achieving a superposition size of 20 μ m with a 10^{-17} kg mass requires a total time of $\tau_6 \approx 1.25$ s, which corresponds to the moderate magnetic field gradient $\eta \sim 46.8$ T m $^{-1}$, again using $B_0 = 10^{-2}$ T and $B_1 = 100\epsilon$, which can be achieved in a laboratory [45,46].

III. SPIN PHASE EVOLUTION

To determine the output signal expected from such an interferometer it is necessary to consider the phase evolution difference between the two paths taken through the interferometer. The final output signal will be the result of a combination of the phase accumulated by the phase due to the path it takes through the interferometer, and external forces acting on the masses, such as gravitational or electromagnetic interactions which differ across the paths taken through the interferometer. For the moment, however, we will neglect these outside sources due to the highly implementation-dependent nature of these. Given that the entire Hamiltonian is used to determine the trajectories, it is sufficient to calculate the action for a *free* spin traveling along a fixed trajectory given by the two trajectories through the interferometer. This will then yield a phase θ accumulated along a path γ of

$$\theta = \frac{1}{\hbar} \int_{\gamma} \frac{p(t)^2}{2m} dt, \quad (12)$$

where $p(t)$ is the time-dependent momentum of the particle. To evaluate this we can approximate the motion as being in three distinct segments: $\tau_0 = 0 \leq t \leq \tau_1$, before the particle has reached the zero-field region; $\tau_2 < t \leq \tau_3$, after the particle has reached the zero-field region but before the spin has been reversed; and $\tau_3 < t \leq \tau_4$, the remainder of the evolution, ending when the two wave packets are brought to overlap. Note that the time region $t \in [\tau_1, \tau_2]$ is extremely brief and does not significantly change the end result. In each of these sections the general particle momentum can be written as

$$p^{+/-}(t) = -m\omega A_i^{+/-} \sin(\omega t + \phi_i^{+/-}) \quad (13)$$

for the + and - arm of the interferometer and the value of $A^{+/-}$ and $\phi^{+/-}$ differs from one segment to the next. Thus the phase difference accumulated through any given stage of the

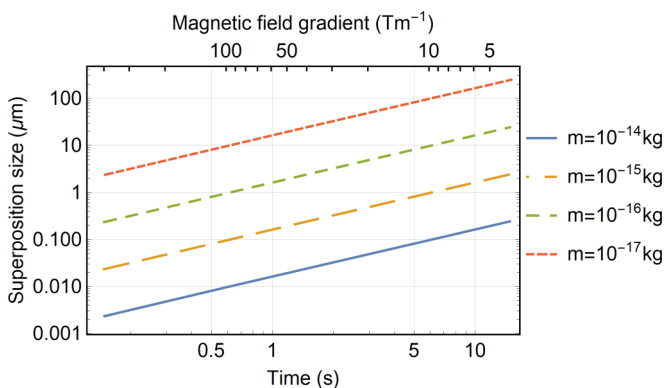


FIG. 3. Superposition size versus time. This shows the maximal superposition size achievable, as determined by the calculated paths. Note that for masses $m = 10^{-17}$ kg and heavier these results are well approximated by Eq. (11).

interferometer will be

$$\begin{aligned}
 \Delta\theta &= \sum_{i \in \{1,3,4\}} \left\{ \frac{m}{2\hbar} \int_{\tau_{i-1}}^{\tau_i} [\omega A_i^+ \sin(\omega t + \phi_i^+)]^2 \right. \\
 &\quad \left. - \frac{m}{2\hbar} \int_{\tau_i}^{\tau_{i+1}} [\omega A_i^- \sin(\omega t + \phi_i^-)]^2 \right\} \\
 &= \frac{m\omega}{8\hbar} [2\omega\tau_1 - \sin(2\omega\tau_1)] [(A_1^+)^2 - (A_1^-)^2] \\
 &\quad + \sum_{i=3}^4 \frac{m}{8\hbar} \left\{ 2\omega^2(T_i - T_{i-1}) [(A^+)^2 - (A^-)^2] \right. \\
 &\quad + \sin(2\phi^+ + 2T_{i-1}\omega) - \sin(2\phi^- + 2T_{i-1}\omega) \\
 &\quad \left. - \sin(2\phi^+ + 2T_i\omega) + \sin(2\phi^- + 2T_i\omega) \right\}. \quad (14)
 \end{aligned}$$

Now it is suitably insightful to consider in detail the phase difference accrued when $t \in [\tau_0, \tau_1]$, noting that $\sin(2\omega\tau_1) \approx 0$:

$$\begin{aligned}
 \Delta\theta(t = \tau_1) &\approx \frac{m}{8\hbar} \{ 2\omega^2\tau_1 [(A_1^+)^2 - (A_1^-)^2] \\
 &\quad - \sin(2\tau_1\omega) + \sin(2\tau_1\omega) \} \\
 &= \frac{m}{8\hbar} 2\omega^2\tau_1 \left[\left(\frac{B_0}{\eta} + \alpha \right)^2 - \left(\frac{B_0}{\eta} - \alpha \right)^2 \right] \\
 &= \frac{geB_0}{2m_e} \tau_1. \quad (15)
 \end{aligned}$$

Given that in each time segment considered here, the particles are simply acting as harmonic oscillators, flipping between two different harmonic wells, the entire path phase difference can be approximated as

$$\Delta\theta \approx \frac{geB_0}{2m_e} \left(\frac{\tau_1}{\tau_4} - \frac{\tau_3 - \tau_1}{\tau_4} + \frac{\tau_4 - \tau_3}{\tau_4} \right) \tau_4, \quad (16)$$

where the extra terms in Eq. (14) are neglected and the negative time scaling occurs when the internal spin direction is reversed relative to the external field. Note that this occurs by reversing the field magnitude, not the particle spin state. This entire term $\left(\frac{\tau_1}{\tau_4} - \frac{\tau_3 - \tau_1}{\tau_4} + \frac{\tau_4 - \tau_3}{\tau_4} \right) \approx 0.5$ can be viewed as a comparison between the time spent with the masses being accelerated away from one another and time spent being attracted toward one another. This would typically be equal and as such this entire phase would not usually appear. It is only due to the asymmetry in this interferometer setup that it occurs. Thus, for the full trajectories, the path phase difference will be $\Delta\theta \propto \tau_4$. This can be seen clearly in Fig. 4, which shows the phase scaling linearly with time and almost independently of mass. This also shows the approximate phase difference given by Eq. (16) and how it compares to the exact values. This also allows for the required stability to be estimated, using Eq. (16): $\Delta\theta \approx \frac{ge}{4m_e} B_0 \tau_4 \sim B_0 \tau_4 \times 10^{11} \text{ T}^{-1} \text{ s}^{-1}$; to keep the final phase uncertainty $\delta(\Delta\theta) < 1$ will require

$$10^{-11} \text{ T s} > B_0 \times \delta t, \quad (17)$$

$$10^{-11} \text{ T s} > \delta B_0 \times t, \quad (18)$$

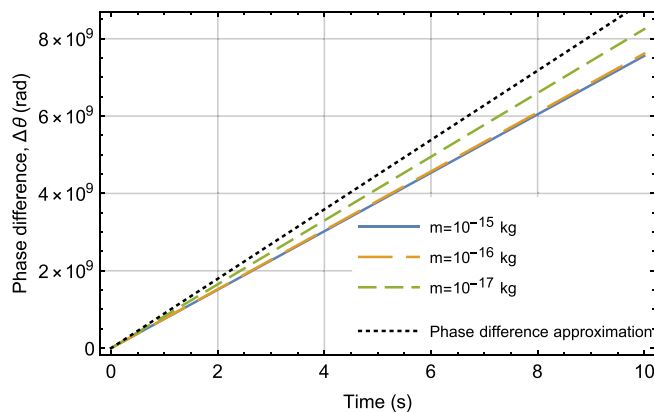


FIG. 4. Phase difference magnitude scaling with total runtime for $m = 10^{-15} \text{ kg}$, $m = 10^{-16} \text{ kg}$, and $m = 10^{-17} \text{ kg}$. This also shows the phase difference as predicted by Eq. (16).

which places a strict requirement on both timing certainty, δt , and bias field stability, δB_0 . This will serve as a further challenge that must be met before such an experiment can be fully realized.

IV. DISCUSSION

In this paper, we have provided a simple mechanism to accelerate heavy neutral masses, with embedded spin, so as to create large spatial superpositions. Using Eq. (11) we estimate that one can create, for example, the spatial superposition of $\sim 20 \mu\text{m}$ for masses as heavy as 10^{-17} kg . Our simple scheme fills the gap required for a realistic “wave function splitting” of large masses to achieve a large spatial superposition, and herewith opens up new vistas for testing and probing both the classical and quantum nature of gravity while also giving access to unprecedented sensing opportunities.

The time duration of coherence, and hence the experiment, is the *only* limiting factor, but (a) spin coherence times are perpetually rising (approaching 1 s [47,48], even 30 s [49,50])—adapting these to nanocrystals remains an open problem, but is not fundamentally restricted [51], and (b) spatial coherence times can be made $\sim 100 \text{ s}$ [2,6,9,10], by challenging but achievable pressures [52], temperatures [53], distances from other sources, and fluctuations. For example, a decoherence rate below 0.1 Hz is achievable for diamond spheres of masses $\sim 10^{-14} \text{ kg}$. This is expected [54] for internal temperatures of 0.15 K, an environmental temperature of 1 K, and an environmental gas number density of 10^8 m^{-3} .

Effort will also have to be taken to initialize the particle with the spin direction aligned with the external applied magnetic field to minimize spurious torques arising from the spin–magnetic field coupling. This can be accomplished already before being released from a trap, for example, by using anisotropically shaped nanoparticles, which can be aligned with any given direction in space by using linearly polarized lasers or electric fields [55] or magnetic fields [56]. There will still be harmonic motion about this orientation axis (called librations), which generally have much higher frequencies [57] than typical center-of-mass trapping frequencies in tweezers. As the latter has already been cooled to the ground state by

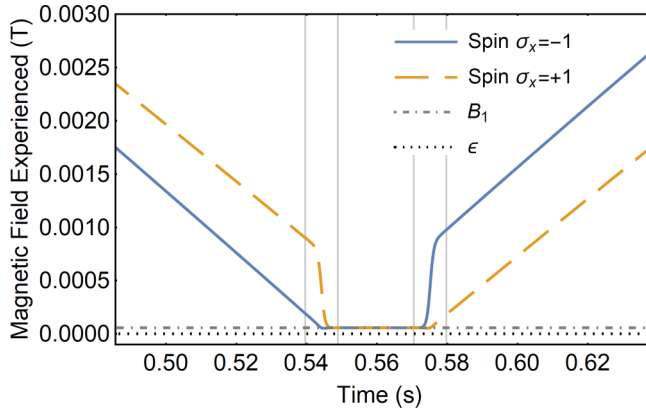


FIG. 5. Magnetic field experienced by each arm of the interferometer with time. The vertical gray lines represent times τ_i for $i = 1, 2, 3, 4$ using $B_0 = 10^{-2}$ T, $\eta = 40$ T m $^{-1}$, and $B_1 = 100\epsilon$ T.

feedback cooling [58–61], one would expect the former (librations) to be possible to be cooled to the ground state also. In fact, these librations have been substantially cooled [62]. Once it is cooled close to the ground state, the spin direction will be effectively exactly aligned to the external magnetic field. If the magnetic field is maintained throughout the interference in the same direction then the spin, and hence the nanoparticle, receives no torque from it. We also note that it has already been shown that the internal degrees of freedom (phonons) do not pose a practical problem [63]. We have shown that there are also requirements on the magnetic field fluctuations and timing certainty to ensure a stable interference signal, both at achievable levels, however [64–67]. To conclude, we have found an explicit scheme to create large spatial superpositions, with the size increasing in proportion to achievable coherence times, but otherwise not limited.

ACKNOWLEDGMENTS

R.J.M. is supported by a EPSRC DTP departmental studentship at UCL. A.M.'s research is funded by the Netherlands Organisation for Science and Research (NWO), Grant No. 680-91-119. R.F. is supported by the Israel Science Foundation. S.B. would like to acknowledge EPSRC Grants No. EP/N031105/1 and No. EP/S000267/1.

APPENDIX: SOLVING THE PARTICLE DYNAMICS

In this Appendix, we provide our analytical and numerical treatment of the equations of motion. The magnetic fields used to create the superposition are

$$\vec{B}(x, y) = (B_0 - \eta x)\hat{x} + \eta y\hat{y}, \quad (\text{A1})$$

$$\vec{B}(x, y) = B_1\hat{x}, \quad (\text{A2})$$

$$\vec{B}(x, y) = -(B_0 - \eta x)\hat{x} - \eta y\hat{y}, \quad (\text{A3})$$

with the magnetic field being mapped between Eqs. (A1) to (A2) when $t \in [\tau_1, \tau_2]$, and between Eqs. (A2) to (A3) when $t \in [\tau_3, \tau_4]$. Figure 5 shows the detail of the experienced magnetic field for each arm of the interferometer during the

period in which the magnetic field is modified. This shows that provided the value chosen for B_1 is sufficiently large, the minimum allowable experienced magnetic field ϵ can be avoided while ensuring a smooth and adiabatic magnetic field transition. When not in this phase ($t \notin [\tau_1, \tau_4]$) the motion is simply governed by the harmonic oscillator potential, whose solution is given by

$$x(t) = A \cos(\omega t + \phi) + C(s_x), \quad (\text{A4})$$

where A and ϕ are determined by the initial conditions, $\omega = \sqrt{-\frac{\chi_m}{\mu_0}\eta}$ is the frequency of the diamagnetic trap, and $C(s_x)$ is determined by the spin states and magnetic field [Eqs. (A1) and (A3)]. Note that we are always within the adiabatic limit throughout these times, such that $\dot{\omega}/\omega^2 < 1$. We also have

$$C^{s_x=\pm 1} = B_0/\eta \pm \alpha, \quad (\text{A5})$$

where $\alpha = -\mu_{\pm} \frac{\mu_0}{\chi_m m \hbar(t)} = -\frac{ge\hbar}{2m_e} \frac{\mu_0}{\chi_m m \hbar(t)}$. The trajectory through these times, $t \notin [\tau_1, \tau_4]$, can be constructed by simply assembling the solutions piecewise. To do this, the values of the constants are given by the function of the initial conditions at each time segment. Specifically, if $x(t_0) = x_0$ and $\dot{x}(t_0) = v_0$ serve as the initial conditions, then

$$A = -(C - x_0) \left[1 + \frac{v_0^2}{\omega^2} (C - x_0)^{-2} \right]^{1/2}, \quad (\text{A6})$$

$$\phi = \tan^{-1} \left(\frac{v_0}{\omega(C - x_0)} \right) - \omega t_0. \quad (\text{A7})$$

For example, if we consider the particle to be initialized in a superposition of spin states $|+1\rangle$ and $|-1\rangle$ at the origin with zero initial velocity, then we can define the initial motion of the two arms as

$$x_1^+(t) = -\left(\frac{B_0}{\eta} + \alpha \right) \cos(\omega t) + \left(\frac{B_0}{\eta} + \alpha \right), \quad (\text{A8})$$

$$x_1^-(t) = -\left(\frac{B_0}{\eta} - \alpha \right) \cos(\omega t) + \left(\frac{B_0}{\eta} - \alpha \right). \quad (\text{A9})$$

When the magnetic field is given by Eq. (A2) there will be no spin-dependant acceleration; that is, there is no force acting to either create or destroy the spatial superposition. Thus we want to minimize $\tau_4 - \tau_1$. To do this, the initial evolution, $x_1(t)$, should be maintained for as long as possible while still ensuring that

$$x \notin \left[\frac{B_x(0, 0) - \epsilon}{\partial B}, \frac{B_x(0, 0) + \epsilon}{\partial B} \right] \quad (\text{A10})$$

is satisfied. Only as the particle approaches the boundary set by Eq. (A10) is the magnetic field modified (this marks the time τ_1). Specifically, this is done as the magnetic field experienced by the forwardmost trajectory approaches B_1 :

$$x_1^+(t \approx \tau_1) = \frac{B_0 - B_1}{\eta}, \quad (\text{A11})$$

where we write $x_1^-(\tau_1) = A_1^- \cos(\omega\tau_1) + C_1^-$.

Similarly, the nonzero magnetic field gradient should be returned as soon as possible while ensuring Eq. (A10) holds. As such, the magnetic field gradient should begin being restored as the magnetic field experienced by the rearmost trajectory

TABLE I. τ_i values used to calculate wave-packet trajectories for example magnetic field gradients (η).

	$\eta = 4 \text{ T m}^{-1}$	$\eta = 40 \text{ T m}^{-1}$	$\eta = 400 \text{ T m}^{-1}$
τ_1	5.39 s	0.534 s	0.0493 s
τ_2	5.39 s	0.539 s	0.0539 s
τ_3	5.80 s	0.580 s	0.0580 s
τ_4	5.80 s	0.584 s	0.0626 s
τ_5	9.01 s	0.902 s	0.0913 s
τ_6	14.8 s	1.48 s	0.148 s

$[x_2^-(t)]$ approximates the magnetic field as given by Eq. (A3), that is,

$$B_1 = -B_0 + \eta x_2^-(\tau_3),$$

$$x_2^-(t \approx \tau_3) = \frac{B_1 - B_0}{\eta}, \tag{A12}$$

where x_2^+ and x_2^- are the trajectories when $t \in [\tau_1, \tau_4]$, and are found by numerically integrating the equations of motion.

The final two stages of the trajectories are given by

$$x_3^+(t) = A_3^+ \cos(\omega t + \phi_3^+) + C_3^+, \tag{A13}$$

$$x_3^-(t) = A_3^- \cos(\omega t + \phi_3^-) + C_3^-, \tag{A14}$$

$$x_4^+(t) = A_4^+ \cos(\omega t + \phi_4^+) + C_4^+, \tag{A15}$$

$$x_4^-(t) = A_4^- \cos(\omega t + \phi_4^-) + C_4^-, \tag{A16}$$

where

$$A_3^+ = -[C_3^+ - x_2^+(\tau_2)] \left\{ 1 + \frac{[v_2^+(\tau_2)]^2}{\omega^2} [C_3^+ - x_2^+(\tau_2)]^{-2} \right\}^{1/2},$$

$$A_3^- = -[C_3^- - x_2^-(\tau_2)] \left\{ 1 + \frac{[v_2^-(\tau_2)]^2}{\omega^2} [C_3^- - x_2^-(\tau_2)]^{-2} \right\}^{1/2},$$

$$\phi_3^+ = \tan^{-1} \left\{ \frac{v_2^+(\tau_2)}{\omega [C_3^+ - x_2^+(\tau_2)]} \right\} - \omega \tau_2,$$

$$\phi_3^- = \tan^{-1} \left\{ \frac{v_2^-(\tau_2)}{\omega [C_3^- - x_2^-(\tau_2)]} \right\} - \omega \tau_2,$$

$$C_3^+ = -\left(\frac{B_0}{\eta} - \alpha \right),$$

$$C_3^- = -\left(\frac{B_0}{\eta} + \alpha \right), \tag{A17}$$

and

$$A_4^+ = -[C_4^+ - x_3^+(\tau_3)] \left\{ 1 + \frac{[v_3^+(\tau_3)]^2}{\omega^2} [C_4^+ - x_3^+(\tau_3)]^{-2} \right\}^{1/2},$$

$$A_4^- = -[C_4^- - x_3^-(\tau_3)] \left\{ 1 + \frac{[v_3^-(\tau_3)]^2}{\omega^2} [C_4^- - x_3^-(\tau_3)]^{-2} \right\}^{1/2},$$

$$\phi_4^+ = \tan^{-1} \left\{ \frac{v_3^+(\tau_3)}{\omega [C_4^+ - x_3^+(\tau_3)]} \right\} - \omega \tau_3,$$

$$\phi_4^- = \tan^{-1} \left\{ \frac{v_3^-(\tau_3)}{\omega [C_4^- - x_3^-(\tau_3)]} \right\} - \omega \tau_3,$$

$$C_4^+ = -\left(\frac{B_0}{\eta} + \alpha \right),$$

$$C_4^- = -\left(\frac{B_0}{\eta} - \alpha \right). \tag{A18}$$

The values for the times τ_5 and τ_6 are fixed by the following conditions:

(1) $\Delta x(\tau_6) = x_4^+(\tau_6) - x_4^-(\tau_6) = 0$ and $\Delta v(\tau_6) = v_4^+(\tau_6) - v_4^-(\tau_6) = 0$, such that the two arms of the interferometers are brought together to overlap in both the position and the momentum space, respectively.

(2) $x_4^+(\tau_6) > \frac{B_0 + \epsilon}{\eta}$, such that the Majorana spin flip region of the magnetic field is again avoided.

Note that the appropriate timescales which met the above conditions (conditions 1 and 2) were found *solely* numerically. This has led to a set of times and the corresponding magnetic field gradients applied during the time period, which we have tabulated in Table I.

There are a couple of points to note here: The time τ_6 , set such that $\Delta v(\tau_6) = 0$, will automatically minimize $\Delta x(\tau_6)$. Also, the value of Δx evaluated at time τ_6 is continuous in τ_5 , and there exist times t_1 and $t_2 \in \mathbb{R}$ such that, when $\tau_5 = t_1$, $\Delta x(\tau_6) > 0$, and when $\tau_5 = t_2$, $\Delta x(\tau_6) < 0$. In a nutshell the procedure to find the correct values of τ_5 and τ_6 is as follows:

(1) Make an initial guess for the value of τ_5 which was used to calculate a complete trajectory; typically this is $\tau_5 = 2\tau_4$.

(2) From this we have evaluated the value of τ_6 , which we have determined using the relation $\Delta v(\tau_6) = 0$.

(3) The corresponding value of $\Delta x(\tau_6)$ was then evaluated. This allows the assumed value for τ_5 to be optimized accordingly. Specifically, note that increasing τ_5 will lead to a decrease in the value of $\Delta x(\tau_6)$.

[1] S. Weinberg, *The Quantum Theory of Fields, Vol. 1: Foundations* (Cambridge University Press, Cambridge, England, 2005).
 [2] S. Bose, A. Mazumdar, G. W. Morley, H. Ulbricht, M. Toroš, M. Paternostro, A. Geraci, P. Barker, M. Kim, and G. Milburn, Spin Entanglement Witness for Quantum Gravity, *Phys. Rev. Lett.* **119**, 240401 (2017).
 [3] R. J. Marshman, A. Mazumdar, and S. Bose, Locality and entanglement in table-top testing of the quantum nature of linearized gravity, *Phys. Rev. A* **101**, 052110 (2020).

[4] C. Marletto and V. Vedral, Gravitationally Induced Entanglement between Two Massive Particles Is Sufficient Evidence of Quantum Effects in Gravity, *Phys. Rev. Lett.* **119**, 240402 (2017).
 [5] T. Biswas, E. Gerwick, T. Koivisto, and A. Mazumdar, Towards Singularity and Ghost Free Theories of Gravity, *Phys. Rev. Lett.* **108**, 031101 (2012).
 [6] T. W. van de Kamp, R. J. Marshman, S. Bose, and A. Mazumdar, Quantum gravity witness via entanglement

- of masses: Casimir screening, *Phys. Rev. A* **102**, 062807 (2020).
- [7] M. Arndt, O. Nairz, J. Vos-Andreae, C. Keller, G. van der Zouw, and A. Zeilinger, Wave particle duality of C_{60} molecules, *Nature (London)* **401**, 680 (1999).
- [8] M. Arndt and K. Hornberger, Testing the limits of quantum mechanical superpositions, *Nat. Phys.* **10**, 271 (2014).
- [9] M. Toroš, T. W. van de Kamp, R. J. Marshman, M. S. Kim, A. Mazumdar, and S. Bose, Relative acceleration noise mitigation for nanocrystal matter-wave interferometry: Applications to entangling masses via quantum gravity, *Phys. Rev. Research* **3**, 023178 (2021).
- [10] R. J. Marshman, A. Mazumdar, G. W. Morley, P. F. Barker, S. Hoekstra, and S. Bose, Mesoscopic interference for metric and curvature (MIMAC) & gravitational wave detection, *New J. Phys.* **22**, 083012 (2020).
- [11] A. J. Leggett, Testing the limits of quantum mechanics: Motivation, state of play, prospects, *J. Phys.: Condens. Matter* **14**, R415 (2002).
- [12] S. Bose, K. Jacobs, and P. L. Knight, Scheme to probe the decoherence of a macroscopic object, *Phys. Rev. A* **59**, 3204 (1999).
- [13] A. D. Armour, M. P. Blencowe, and K. C. Schwab, Entanglement and Decoherence of a Micromechanical Resonator via Coupling to a Cooper-Pair Box, *Phys. Rev. Lett.* **88**, 148301 (2002).
- [14] W. Marshall, C. Simon, R. Penrose, and D. Bouwmeester, Towards Quantum Superpositions of a Mirror, *Phys. Rev. Lett.* **91**, 130401 (2003).
- [15] P. Sekatski, M. Aspelmeyer, and N. Sangouard, Macroscopic Optomechanics from Displaced Single-Photon Entanglement, *Phys. Rev. Lett.* **112**, 080502 (2014).
- [16] O. Romero-Isart, M. L. Juan, R. Quidant, and J. I. Cirac, Toward quantum superposition of living organisms, *New J. Phys.* **12**, 033015 (2010).
- [17] O. Romero-Isart, A. C. Pflanzer, F. Blaser, R. Kaltenbaek, N. Kiesel, M. Aspelmeyer, and J. I. Cirac, Large Quantum Superpositions and Interference of Massive Nanometer-Sized Objects, *Phys. Rev. Lett.* **107**, 020405 (2011).
- [18] F. Khalili, S. Danilishin, H. Miao, H. Müller-Ebhardt, H. Yang, and Y. Chen, Preparing a Mechanical Oscillator in Non-Gaussian Quantum States, *Phys. Rev. Lett.* **105**, 070403 (2010).
- [19] M. Scala, M. S. Kim, G. W. Morley, P. F. Barker, and S. Bose, Matter-Wave Interferometry of a Levitated Thermal Nano-Oscillator Induced and Probed by a Spin, *Phys. Rev. Lett.* **111**, 180403 (2013).
- [20] C. Wan, M. Scala, G. W. Morley, A. A. Rahman, H. Ulbricht, J. Bateman, P. F. Barker, S. Bose, and M. S. Kim, Free Nano-Object Ramsey Interferometry for Large Quantum Superpositions, *Phys. Rev. Lett.* **117**, 143003 (2016).
- [21] J. Bateman, S. Nimmrichter, K. Hornberger, and H. Ulbricht, Near-field interferometry of a free-falling nanoparticle from a point-like source, *Nat. Commun.* **5**, 4788 (2014).
- [22] Z. Q. Yin, T. Li, X. Zhang, and L. M. Duan, Large quantum superpositions of a levitated nanodiamond through spin-optomechanical coupling, *Phys. Rev. A* **88**, 033614 (2013).
- [23] H. Pino, J. Prat-Camps, K. Sinha, B. P. Venkatesh, and O. Romero-Isart, On-chip quantum interference of a superconducting microsphere, *Quantum Sci. Technol.* **3**, 025001 (2018).
- [24] J. Clarke and M. R. Vanner, Growing macroscopic superposition states via cavity quantum optomechanics, *Quantum Sci. Technol.* **4**, 014003 (2019).
- [25] M. Ringbauer, T. J. Weinhold, L. Howard, A. White, and M. Vanner, Generation of mechanical interference fringes by multiphoton counting, *New J. Phys.* **20**, 053042 (2018).
- [26] K. E. Khosla, M. R. Vanner, N. Ares, and E. A. Laird, Displacement Electromechanics: How to Detect Quantum Interference in a Nanomechanical Resonator, *Phys. Rev. X* **8**, 021052 (2018).
- [27] R. Kaltenbaek, G. Hechenblaikner, N. Kiesel, O. Romero-Isart, K. C. Schwab, U. Johann, and M. Aspelmeyer, Macroscopic quantum resonators (MAQRO), *Exp. Astron.* **34**, 123 (2012).
- [28] O. Romero-Isart, Coherent inflation for large quantum superpositions of levitated microspheres, *New J. Phys.* **19**, 123029 (2017).
- [29] J. S. Pedernales, G. W. Morley, and M. B. Plenio, Motional Dynamical Decoupling for Interferometry with Macroscopic Particles, *Phys. Rev. Lett.* **125**, 023602 (2020).
- [30] *Atom Optics and Space Physics: Proceedings of the International School of Physics "Enrico Fermi"*, edited by E. Arimondo, W. Ertmer, W. Schleich, and E. M. Rasel (IOS Press, Amsterdam, 2009).
- [31] Y. Margalit, O. Dobkowski, Z. Zhou, O. Amit, Y. Japha, S. Moukouri, D. Rohrich, A. Mazumdar, S. Bose, C. Henkel, et al., Realization of a complete Stern-Gerlach interferometer: Toward a test of quantum gravity, *Sci. Adv.* **7**, eabg2879 (2021).
- [32] A. Al Balushi, W. Cong, and R. B. Mann, Optomechanical quantum Cavendish experiment, *Phys. Rev. A* **98**, 043811 (2018).
- [33] A. Bassi, K. Lochan, S. Satin, T. P. Singh, and H. Ulbricht, Models of wave-function collapse, underlying theories, and experimental tests, *Rev. Mod. Phys.* **85**, 471 (2013).
- [34] T. Kovachy, P. Asenbaum, C. Overstreet, C. Donnelly, S. Dickerson, A. Sugarbaker, J. Hogan, and M. Kasevich, Quantum superposition at the half-metre scale, *Nature (London)* **528**, 530 (2015).
- [35] J. Murata and S. Tanaka, A review of short-range gravity experiments in the LHC era, *Class. Quantum Gravity* **32**, 033001 (2015).
- [36] C. Wan, Quantum superposition on nano-mechanical oscillator, Ph.D. thesis, Imperial College London, 2017.
- [37] M. M. Paraniak and B.-G. Englert, Quantum dynamical simulation of a transversal stern-gerlach interferometer, *Symmetry* **13**, 1660 (2021).
- [38] E. Majorana, Atomi orientati in campo magnetico variabile, *Nuovo Cimento* **9**, 43 (1932).
- [39] M. Inguscio, Majorana "spin-flip" and ultra-low temperature atomic physics, *PoS EMC2006*, 008 (2006).
- [40] J. H. N. Loubser and J. A. van Wyk, Electron spin resonance in the study of diamond, *Rep. Prog. Phys.* **41**, 1201 (1978).
- [41] S. Kuhn, A. Kosloff, B. A. Stickler, F. Patolsky, K. Hornberger, M. Arndt, and J. Millen, Full rotational control of levitated silicon nanorods, *Optica* **4**, 356 (2017).
- [42] J. Schäfer, H. Rudolph, K. Hornberger, and B. A. Stickler, Cooling Nanorotors by Elliptic Coherent Scattering, *Phys. Rev. Lett.* **126**, 163603 (2021).
- [43] H. Rudolph, J. Schäfer, B. A. Stickler, and K. Hornberger, Theory of nanoparticle cooling by elliptic coherent scattering, *Phys. Rev. A* **103**, 043514 (2021).

- [44] F. van der Laan, F. Tebbenjohanns, R. Reimann, J. Vijayan, L. Novotny, and M. Frimmer, Sub-Kelvin Feedback Cooling and Heating Dynamics of an Optically Levitated Librator, *Phys. Rev. Lett.* **127**, 123605 (2021).
- [45] S. Machluf, Y. Japha, and R. Folman, Coherent Stern-Gerlach momentum splitting on an atom chip, *Nat. Commun.* **4**, 2424 (2013).
- [46] M. Modena, J. Garcia Perez, P. Thonet, C. Petrone, A. Vorozhtsov, O. Dunkel, E. Solodko, and D. Tommasini, Design, assembly and first measurements of a short model for CLIC final focus hybrid quadrupole QD0, *Conf. Proc.* **1205201**, THPPD010 (2012).
- [47] N. Bar-Gill, L. M. Pham, A. Jarmola, D. Budker, and R. L. Walsworth, Solid-state electronic spin coherence time approaching one second, *Nat. Commun.* **4**, 1743 (2013).
- [48] M. H. Abobeih, J. Cramer, M. A. Bakker, N. Kalb, M. Markham, D. J. Twitchen, and T. H. Taminiou, One-second coherence for a single electron spin coupled to a multi-qubit nuclear-spin environment, *Nat. Commun.* **9**, 2552 (2018).
- [49] J. T. Muhonen, J. P. Dehollain, A. Laucht, F. E. Hudson, R. Kalra, T. Sekiguchi, K. M. Itoh, D. N. Jamieson, J. C. McCallum, A. S. Dzurak *et al.*, Storing quantum information for 30 seconds in a nanoelectronic device, *Nat. Nanotechnol.* **9**, 986 (2014).
- [50] D. Farfurnik, A. Jarmola, L. M. Pham, Z.-H. Wang, V. V. Dobrovitski, R. L. Walsworth, D. Budker, and N. Bar-Gill, Optimizing a dynamical decoupling protocol for solid-state electronic spin ensembles in diamond, *Phys. Rev. B* **92**, 060301(R) (2015).
- [51] H. S. Knowles, D. M. Kara, and M. Atatüre, Observing bulk diamond spin coherence in high-purity nanodiamonds, *Nat. Mater.* **13**, 21 (2014).
- [52] D. Fitzakerley, M. George, E. Hessels, T. Skinner, C. Storry, M. Weel, G. Gabrielse, C. Hamley, N. Jones, K. Marable *et al.*, Electron-cooled accumulation of 4×10^9 positrons for production and storage of antihydrogen atoms, *J. Phys. B: At., Mol. Opt. Phys.* **49**, 064001 (2016).
- [53] A. Marx, J. Hoess, and K. Uhlig, Dry dilution refrigerator for experiments on quantum effects in the microwave regime, [arXiv:1412.3619](https://arxiv.org/abs/1412.3619).
- [54] M. Schut, J. Tilly, R. J. Marshman, S. Bose, and A. Mazumdar, Improving resilience of the quantum gravity induced entanglement of masses to decoherence using three superpositions, *Phys. Rev. A* **105**, 032411 (2022).
- [55] B. A. Stickler, K. Hornberger, and M. Kim, Quantum rotations of nanoparticles, *Nat. Rev. Phys.* **3**, 589 (2021).
- [56] A. A. Wood, R. M. Goldblatt, R. E. Scholten, and A. M. Martin, Quantum control of nuclear-spin qubits in a rapidly rotating diamond, *Phys. Rev. Research* **3**, 043174 (2021).
- [57] S. Liu, T. Li, and Z.-q. Yin, Coupling librational and translational motion of a levitated nanoparticle in an optical cavity, *J. Opt. Soc. Am. B* **34**, C8 (2017).
- [58] F. Tebbenjohanns, M. L. Mattana, M. Rossi, M. Frimmer, and L. Novotny, Quantum control of a nanoparticle optically levitated in cryogenic free space, *Nature (London)* **595**, 378 (2021).
- [59] U. Delić, M. Reisenbauer, K. Dare, D. Grass, V. Vuletić, N. Kiesel, and M. Aspelmeyer, Cooling of a levitated nanoparticle to the motional quantum ground state, *Science* **367**, 892 (2020).
- [60] F. Tebbenjohanns, M. Frimmer, V. Jain, D. Windey, and L. Novotny, Motional Sideband Asymmetry of a Nanoparticle Optically Levitated in Free Space, *Phys. Rev. Lett.* **124**, 013603 (2020).
- [61] L. Magrini, P. Rosenzweig, C. Bach, A. Deutschmann-Olek, S. G. Hofer, S. Hong, N. Kiesel, A. Kugi, and M. Aspelmeyer, Real-time optimal quantum control of mechanical motion at room temperature, *Nature (London)* **595**, 373 (2021).
- [62] T. Delord, P. Huillery, L. Nicolas, and G. Hétet, Spin-cooling of the motion of a trapped diamond, *Nature (London)* **580**, 56 (2020).
- [63] C. Henkel and R. Folman, Internal decoherence in nano-object interferometry due to phonons, [arXiv:2112.01263](https://arxiv.org/abs/2112.01263).
- [64] T. Ruster, C. T. Schmiegelow, H. Kaufmann, C. Warschburger, F. Schmidt-Kaler, and U. G. Poschinger, A long-lived Zeeman trapped-ion qubit, *Appl. Phys. B* **122**, 254 (2016).
- [65] C. Gohil, P. Burrows, N. B. Kraljevic, D. Schulte, and B. Heilig, Measurements of sub-nT dynamic magnetic field shielding with soft iron and mu-metal for use in linear colliders, *J. Instrum.* **15**, P12030 (2020).
- [66] I. Sochnikov, D. Davino, and B. Kalisky, dc SQUID Design with Femtotesla Sensitivity for Quantum-Ready Readouts, *Phys. Rev. Appl.* **14**, 014020 (2020).
- [67] G. Mourou, C. Stancampiano, A. Antonetti, and A. Orszag, Picosecond microwave pulses generated with a subpicosecond laser-driven semiconductor switch, *Appl. Phys. Lett.* **39**, 295 (1981).